

## Advanced SQUID-on-lever scanning probe for high-sensitivity magnetic microscopy with sub-100-nm spatial resolution

Timur Weber<sup>1,\*</sup>, Daniel Jetter<sup>2,\*</sup>, Jan Ullmann<sup>1</sup>, Simon A. Koch<sup>1</sup>, Simon F. Pfander<sup>1</sup>, Katharina Kress<sup>2</sup>, Andriani Vervelaki<sup>2</sup>, Boris Gross<sup>2</sup>, Oliver Kieler<sup>3</sup>, Ute Drechsler<sup>4</sup>, Priya R. Baral<sup>5</sup>, Arnaud Magrez<sup>5</sup>, Reinhold Kleiner<sup>1</sup>, Armin W. Knoll<sup>4</sup>, Martino Poggio<sup>2,6</sup> and Dieter Koelle<sup>1,†</sup>

<sup>1</sup>*Physikalisches Institut, Center for Quantum Science (CQ) and LISA<sup>+</sup>, University of Tübingen, 72076 Tübingen, Germany*


<sup>2</sup>*Department of Physics, University of Basel, 4056 Basel, Switzerland*

<sup>3</sup>*Department Quantum Electronics, Physikalisch-Technische Bundesanstalt (PTB), 38116 Braunschweig, Germany*

<sup>4</sup>*IBM Research Europe—Zürich, 8803 Rüschlikon, Switzerland*

<sup>5</sup>*Institute of Physics, École Polytechnique Fédérale de Lausanne, 1015 Lausanne, Switzerland*

<sup>6</sup>*Swiss Nanoscience Institute, University of Basel, 4056 Basel, Switzerland*

 (Received 3 August 2025; revised 4 October 2025; accepted 17 October 2025; published 14 November 2025)

Superconducting quantum interference devices (SQUIDs) are exceptionally sensitive magnetometers, capable of detecting weak magnetic fields. Miniaturizing these devices and integrating them onto scanning probes enables high-resolution imaging at low temperatures. Here, we fabricate nanometer-scale niobium SQUIDs with inner-loop sizes down to 10 nm at the apex of individual planar silicon cantilevers via a combination of wafer-scale optical lithography and focused ion beam (FIB) milling. These robust SQUID-on-lever probes overcome many of the limitations of existing devices, achieving spatial resolution better than 100 nm, magnetic flux sensitivity of  $0.3 \mu\Phi_0/\sqrt{\text{Hz}}$ , and operation in magnetic fields up to about 0.5 T at 4.2 K. Nanopatterning via Ne- or He-FIB milling allows for the incorporation of a modulation line for coupling magnetic flux into the SQUID or a third Josephson junction, for shifting its phase. Such advanced functionality, combined with high spatial resolution, large magnetic field range, and the ease of use of a cantilever-based scanning probe, extends the applicability of scanning SQUID microscopy to a wide range of magnetic, normally conducting, superconducting, and quantum Hall systems. We demonstrate magnetic imaging of skyrmions at the surface of bulk  $\text{Cu}_2\text{OSeO}_3$ . Analysis of the point spread function determined from imaging a single skyrmion yields a full width at half maximum of 71 nm. Moreover, we image modulated magnetization patterns with a period of 65 nm.

DOI: [10.1103/6s24-vz3k](https://doi.org/10.1103/6s24-vz3k)

### I. INTRODUCTION

Magnetic microscopy—because of its ability to reveal magnetization patterns and current distributions—is crucial for studying the properties of magnetic, normally conducting, and superconducting materials. Unlike bulk measurements, which integrate over entire samples, magnetic imaging reveals information about length scales, inhomogeneities, and interactions. A wide variety of techniques, including scanning probe microscopy, light microscopy, and electron microscopy, are available for an even wider variety of materials and conditions [1]. Scanning superconducting quantum interference device (SQUID) microscopy

(SSM) is particularly well-suited for sensitive and high-resolution imaging of transport and magnetization at low temperatures.

In recent years, SSM has been used to explore magnetism in nanostructures [2,3], at complex oxide interfaces [4–6], in topological insulators [7], and in few-layer two-dimensional (2D) magnets [8–11], as well as allowing for the imaging of orbital magnetism in bilayer graphene [12]. SSM was also used to image current flow in both a quantum spin Hall [13] and a quantum anomalous Hall insulator [14], in graphene in the quantum Hall regime [15], in magic-angle twisted bilayer graphene [16], at oxide domain walls [17], and in  $\text{WTe}_2$  in a regime where electrons flow hydrodynamically [18]. In the area of superconductivity, SSM has long been a central tool for discovery, e.g., of the nature of the order parameter symmetry in

\*These authors contributed equally to this work.

†Contact author: koelle@uni-tuebingen.de

cuprate superconductors [19,20]. Most recently, SSM was used to observe the flow of superconducting vortices in a Pb film [21] and quantum fluctuations near criticality in NbTiN [22]. It enabled the discovery of a hidden magnetic phase above the superconducting transition temperature of the van der Waals superconductor 4Hb-TaS<sub>2</sub> [23], as well as vortex excitations carrying a temperature-dependent fraction of the flux quantum  $\Phi_0$  [24].

At the moment, there are two main types of high-resolution SSM. The first is based on a so-called SQUID-on-chip sensor, in which the superconducting device is fabricated via standard lithography on a chip, and a small spatially separated pick-up loop, often at the corner of the chip, couples the sensor to the sample of interest [25–27]. These SQUIDs can be fabricated in large quantities and have the advantage of including on-chip circuitry, such as flux modulation coils and a coil for magnetic susceptibility measurements. However, their spatial resolution is typically in the micrometer range, owing to the size of the pick-up loop and limitations on the minimum SQUID-to-sample distance [19]; moreover, they only function in magnetic fields up to about 10 mT, because of the properties of the Nb/AlO<sub>x</sub>/Nb Josephson junctions (JJs) [28]. A second type of sensor, known as a SQUID-on-tip, consists of a SQUID loop that is fabricated directly at the apex of a quartz capillary via a three-step deposition of superconducting material [29,30]. The JJs of these SQUIDs are Dayem bridges (or constriction junctions), allowing for SQUIDs with diameters less than 100 nm and critical fields in the tesla range [31]. This combination results in SSM probes with submicrometer spatial resolution that operate in a high magnetic field beyond 1 T. However, the process by which SQUID-on-tip sensors are fabricated precludes the application of conventional wafer-scale processing and the integration of circuitry such as a modulation coil for controlling the flux coupling into the SQUID or for local magnetic susceptibility measurements. Moreover, the choice of superconducting material is limited by the nonplanar surfaces on which it must be deposited or grown. Magnetic flux sensitivities of both types of SSM probe typically range from hundreds of  $n\Phi_0/\sqrt{\text{Hz}}$  to a few  $\mu\Phi_0/\sqrt{\text{Hz}}$  at 4.2 K [32].

Recently, nanometer-scale SQUIDs based on Dayem bridge JJs have been realized at the tips of modified commercial Si cantilevers for atomic force microscopy (AFM) using a process based on focused ion beam milling (FIB) [33,34]. Here, we go significantly beyond this initial proof of concept by realizing Nb nanoSQUIDs that are integrated on custom-made Si cantilevers. We use wafer-scale thin-film deposition and optical lithography to produce cantilever chips that contain prepatterned Nb microstructures on planar cantilevers. We combine this with a final FIB milling step, to fabricate sensors reproducibly and in large quantities. This process yields robust SQUID-on-lever sensors that allow for a well-controlled surface

approach, magnetic imaging with spatial resolution better than 100 nm, a magnetic flux sensitivity of  $0.3 \mu\Phi_0/\sqrt{\text{Hz}}$ , operation in magnetic fields up to  $\sim 0.5$  T, and the integration of on-tip circuitry, including a modulation line or a third JJ to flux-bias or phase-bias the devices at the optimum working point. We demonstrate the capabilities of these sensors by imaging nanometer-scale magnetic configurations at the surface of the chiral magnet Cu<sub>2</sub>OSeO<sub>3</sub>. Endowed with the advantages of both SQUID-on-chip and SQUID-on-tip sensors, the resulting probes promise to expand the reach of SSM to a variety of nanometer-scale magnetic, normally conducting, and superconducting systems.

## II. SENSOR FABRICATION AND LAYOUT

We fabricate the probes shown in Fig. 1 on 4 in. silicon-on-insulator (SOI) wafers, resulting in approximately 500 cantilever chips per wafer. Each chip has a size of nominally  $4 \times 1.5 \text{ mm}^2$  [see Fig. 1(a)]. This wafer-scale process starts with a thermal oxidation step, which results in a 50-nm-thick silicon-oxide layer at the surface. Next, we sputter 50 nm of Nb, capped with a 10-nm-thick protective layer of alumina (Al<sub>2</sub>O<sub>3</sub>). We then pattern the Nb film, cantilever, and chip body via optical lithography and reactive ion etching (RIE). To define the Nb microstructures, we use Cl<sub>2</sub>/BCl<sub>3</sub>/Ar, Cl<sub>2</sub>/Ar, and Ar/CHF<sub>3</sub> RIE to etch the alumina, Nb, and thermal oxide, respectively. We use SF<sub>6</sub>/C<sub>4</sub>F<sub>8</sub> deep RIE to etch both the cantilever shape out of the Si device layer and the chip body from the backside, using the buried oxide of the SOI wafer as an etch stop. Finally, we release the cantilevers by removing the buried oxide locally using buffered HF. The resulting cantilevers are about 60  $\mu\text{m}$  long, 40  $\mu\text{m}$  wide, and 2  $\mu\text{m}$  thick, with a spring constant of  $\sim 45 \text{ N/m}$ . As shown in Figs. 1(b) and 1(c), the cantilevers include patterned Nb leads connecting to a triangular device area at the apex of the probe. Seven Nb lines are routed to accommodate multiple layout variants; here, only five are used, and the two outer lines intentionally end before the tip and remain electrically unused.

At the apex of each cantilever, we then pattern the final sensing circuit using high-resolution Ne- and He-FIB milling. First, we use Ne-FIB milling to shape the cantilever tip for optimal AFM operation. If required, we can also remove Nb around the sensing area and the edges of the film. This removes material damaged by the etching process, further limits flux-focusing effects, and prevents the entrance of superconducting vortices close to the SQUID during operation in an applied magnetic field. Once the tip and sensor area have been milled to the appropriate geometry, a specific pattern is applied to fabricate the intended SQUID circuit. By milling away Nb, we define physical gaps in the superconducting film, allowing us to pattern superconducting leads, loops, and Dayem

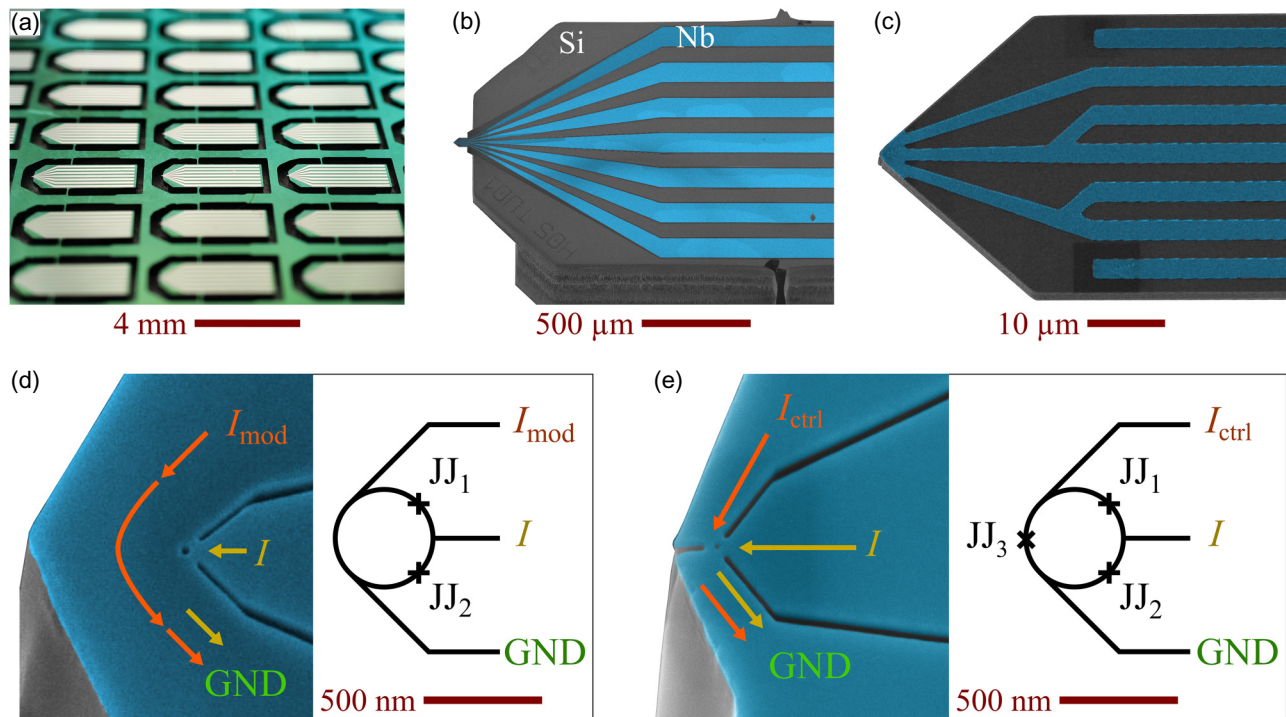


FIG. 1. Planar SQUID-on-lever probe with advanced functionality. (a) Optical micrograph of part of an SOI wafer with 21 patterned cantilever chips, which can be individually broken out. (b) False-colored scanning electron micrograph of part of a cantilever chip with patterned Nb lines extending to the cantilever (left), which protrudes beyond the chip body. (c) False-colored scanning electron micrograph of a cantilever. Three Nb lines (blue) connect to a Nb triangle at the apex (left). (d, e) False-colored scanning electron micrographs (left) and corresponding circuit diagrams (right) illustrate examples of SQUID circuits that were subsequently patterned via Ne- and He-FIB milling by cutting trenches and a hole [diameter  $d = 36$  nm in (d) and 19 nm in (e)] into the Nb triangle. In (d), a modulation current  $I_{\text{mod}}$  can be applied to couple flux into the two-JJ SQUID. In (e) a control current  $I_{\text{ctrl}}$  can be used to shift the phase of the three-JJ SQUID. Each scanning electron micrograph has been taken at an angle of  $45^\circ$ .

bridge JJs. As part of the patterning procedure, we measure and correct for thermal and mechanical drift of the ion beam, to avoid blurring of the desired features.

From studies of the dependence of the critical current  $I_c$  on the width  $w$  of a single JJ, we find that we can realize JJs with  $w$  down to  $\sim 30$  nm via Ne-FIB milling, while with He-FIB milling we can produce JJs with even smaller  $w$ —down to  $\sim 10$  nm—before  $I_c$  drops to zero at 4.2 K [35]. It seems that He-FIB milling produces less edge damage than Ne-FIB milling, i.e., He-FIB milling allows us to realize smaller holes and narrower JJs with reasonable  $I_c$ , at the cost of lower milling rates. This process results in geometric features as small as 10 nm.

The triangular Nb structure at the apex of the cantilever is connected by three Nb lines [see Fig. 1(c)], which are defined by two lithographically patterned trenches between them. To pattern a SQUID with two JJs [ $JJ_1$  and  $JJ_2$ —see Fig. 1(d)], we extend those two trenches by FIB milling toward the cantilever tip. We then mill a SQUID hole with diameter  $d$  between them. The distance between the SQUID hole and each trench defines the widths  $w_1$  and  $w_2$  of  $JJ_1$  and  $JJ_2$ , respectively. The Ne-FIB-cut trenches are 50 nm wide up to a few hundred nanometers from

the SQUID hole, where they are reduced to a width of 25 nm. The final width of the trenches near the SQUID hole defines the length of the Dayem bridge JJs. Using He-FIB milling, the widths of the trenches can be reduced to 15 nm for the last 50–70 nm.

For readout, a bias current  $I$  flows from the central Nb line through the JJs to ground, shown in Fig. 1(d) as the bottom Nb line. In addition, a modulation current  $I_{\text{mod}}$  can be sent from the upper Nb line—flowing along part of the SQUID loop—to ground. When the SQUID is operated in the finite voltage state, the modulation current does not flow across the junctions. Via  $I_{\text{mod}}$ , the SQUID can be flux-biased and operated in a flux-locked loop (FLL).

With a small modification, i.e., by adding a third FIB cut, which runs from the apex toward the SQUID hole, the layout described can be converted into a SQUID with three JJs [see Fig. 1(e)] [36–38]. In that case, we denote the current that flows from the upper Nb line to ground as the control current  $I_{\text{ctrl}}$ . In general, both  $I$  and  $I_{\text{ctrl}}$  can flow across all three JJs. For fixed  $I$ , the control current shifts the phase differences  $\delta_i$  of the superconducting order parameter across the three junctions  $JJ_i$  in the SQUID loop. The control current thus provides a phase bias that can be

used to shift the dependence of the critical current  $I_c$  on the applied flux  $\Phi$  or of the voltage  $V$  on  $\Phi$ . This feature can be implemented in a phase-locked loop (PLL) to keep the SQUID at its optimum working point. For more details on the three-JJ SQUID response, in particular in the voltage state, we refer to Ref. [38].

### III. ELECTRICAL CHARACTERIZATION

The electrical properties and magnetic field response of the SQUID-on-lever (SoL) sensors are characterized at temperature  $T = 4.2$  K. A magnetic field  $B_a = \mu_0 H_a$  is applied perpendicular to the thin-film plane. From around 40 FIB-milled devices, 35 were characterized and all of them showed SQUID oscillations. Next, we present and discuss results obtained with two representative sensors: the first is a SQUID-on-lever with two JJs (2JJ-SoL), which includes a modulation line and was patterned via Ne-FIB milling; the second is a SQUID-on-lever with three JJs (3JJ-SoL), patterned via both Ne- and He-FIB milling to obtain a very small SQUID hole diameter.

Figure 2 summarizes results from four-point measurements of current  $I$  versus voltage  $V$  characteristics (IVCs) of the 2JJ-SoL with a hole diameter  $d = 36$  nm. The two JJs originally had a width  $w_{1,2} = 55$  nm; in a second Ne-FIB milling step (recut), we reduced the JJ widths to  $w_1 = 48$  nm and  $w_2 = 42$  nm, to reduce hysteresis in the IVCs. We note that the quoted JJ widths are nominal widths based on scanning electron microscopy (SEM), which do not include the reduction in effective JJ width due to edge damage induced by Ne-FIB milling. Based on the scaling of experimentally determined critical currents with geometric JJ width  $w$  for our 2JJ-SoLs cut by Ne-FIB milling, we estimate that the degradation of superconductivity extends laterally from the milled edges into the

superconductor by a damage depth of around 15–20 nm; this effectively reduces the JJ widths by around 30–40 nm.

Figure 2(a) shows the oscillation of the critical current  $I_c$  versus modulation current  $I_{\text{mod}}$  before (gray curves) and after (black curves) recutting for both current polarities. In the following, we analyze those patterns, in particular with respect to the determination of the dimensionless screening parameter  $\beta_L \equiv 2LI_0/\Phi_0$  (with SQUID inductance  $L$ , magnetic flux quantum  $\Phi_0 \approx 2.068 \times 10^{-15}$  Vs, and noise-free critical current  $I_0 \approx I_{c,\text{max}}/2$  per JJ) [39,40].

Before recutting, the positive branches of the  $I_c(I_{\text{mod}})$  curves yield maximum and minimum critical currents  $I_{c,\text{max}}^+ = 135 \mu\text{A}$  (at  $I_{\text{mod}} = -185 \mu\text{A}$ ) and  $I_{c,\text{min}}^+ = 67 \mu\text{A}$  (at  $I_{\text{mod}} = 1.2$  mA), respectively; this corresponds to a normalized modulation depth  $\Delta i_c^+ = (I_{c,\text{max}}^+ - I_{c,\text{min}}^+)/I_{c,\text{max}}^+ = 0.50$ . As a first-order approximation, numerical simulations for a symmetric SQUID with a sinusoidal current-phase relation (CPR) of the JJs and negligible thermal noise, predict that  $\Delta i_c^+ = 0.5$  would correspond to  $\beta_L = 1$  [39,40]. The oscillation period  $\Delta I_{\text{mod}} = 2.8$  mA of the  $I_c(I_{\text{mod}})$  curves corresponds to a flux change of  $\Phi_0$  in the SQUID. Accordingly, the mutual inductance of the modulation line is given by  $M = \Phi_0/\Delta I_{\text{mod}} = 0.74$  pH. The relative shift  $\Delta\Phi/\Phi_0 \approx 0.13$  of the  $I_c$  oscillations for both polarities along the flux axis can be attributed to a critical current asymmetry  $\alpha_I$  in the two JJs with critical currents  $I_{c,i} = I_0(1 \pm \alpha_I)$  ( $i = 1, 2$ ), with  $\Delta\Phi/\Phi_0 = \alpha_I\beta_L$  (for negligible inductance asymmetry) [40]. Both an  $I_c$  asymmetry and a deviation from a sinusoidal CPR reduce the modulation depth of  $I_c(\Phi)$  [39,41], which means that this estimate of  $\beta_L = 1$  (and hence the estimate of  $L$ ) is likely to be too large. This indeed seems to be the case, as the measured  $I_{c,\text{max}} = 135 \mu\text{A}$  and  $\beta_L = 1$  yield  $L = 15$  pH, whereas our numerical simulations of the circulating supercurrent distribution [42] for the given SQUID geometry (with London penetration depth  $\lambda_L = 110$  nm) predict

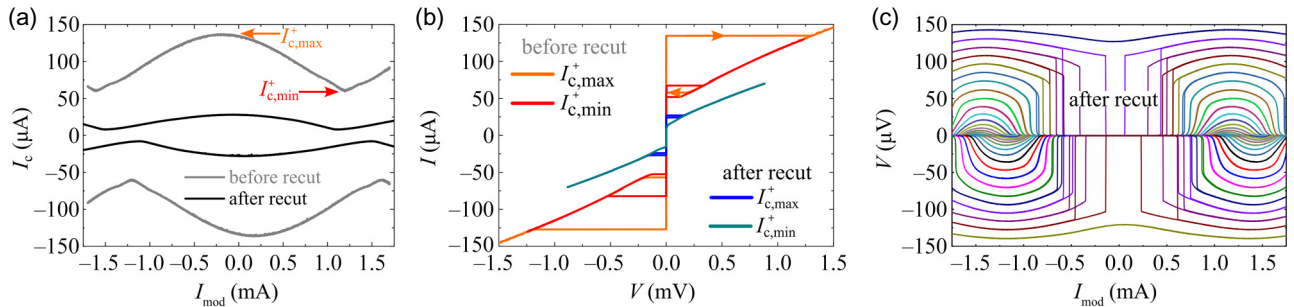


FIG. 2. Electric transport properties of two-JJ SQUID-on-lever probe. Four-point measurements at  $T = 4.2$  K for a SQUID milled by Ne-FIB with hole diameter  $d = 36$  nm and JJ widths  $w_1 = w_2 = 55$  nm before and  $w_1 = 48$  nm and  $w_2 = 42$  nm after recutting by Ne-FIB. (a) Critical current  $I_c$  versus modulation current  $I_{\text{mod}}$  before and after recutting JJs. Arrows indicate maximum and minimum positive critical currents  $I_{c,\text{max}}^+$  and  $I_{c,\text{min}}^+$ , respectively. Curves are shown for both bias current polarities. (b) Current-voltage characteristics before and after recutting, recorded at  $I_{\text{mod}}$  values that provide  $I_{c,\text{max}}^+$  and  $I_{c,\text{min}}^+$ . Before recutting, the IVCs show a pronounced hysteresis (arrows indicate sweep direction of current), which is almost absent after recutting. (c) Voltage  $V$  versus  $I_{\text{mod}}$  oscillations, measured after recutting for different bias currents (from  $-25$  to  $25 \mu\text{A}$  in  $1 \mu\text{A}$  steps).

$L = 1.1$  pH without edge damage and  $L = 2.8$  (2.1) pH with 20 (15) nm damage depth. Those much lower values for  $L$  are consistent with the measured  $M = 0.74$  pH, which is expected to be a significant fraction of  $L$  and result in an estimated  $\beta_L \approx 0.07$  without edge damage and 0.18 (0.13) with 20 (15) nm damage depth.

After recutting, the critical currents are significantly reduced to  $I_{c,\max}^+ = 27$   $\mu$ A (at  $I_{\text{mod}} = -60$   $\mu$ A) and  $I_{c,\min}^+ = 8$   $\mu$ A (at  $I_{\text{mod}} = 1.1$  mA). This yields a normalized modulation depth  $\Delta i_c^+ = 0.70$ ; for a symmetric SQUID with sinusoidal CPR of the JJs and negligible thermal noise, this would correspond to  $\beta_L = 0.42$ . From the slightly reduced oscillation period  $\Delta I_{\text{mod}} = 2.6$  mA of the  $I_c(I_{\text{mod}})$  curves, we extract a slightly increased  $M = 0.8$  pH. A relative shift  $\Delta\Phi/\Phi_0 \approx 0.05$  of the  $I_c$  oscillations for both polarities indicates a finite critical current asymmetry. Again, we expect that  $\beta_L$  is much smaller than 0.42, owing to  $I_c$  asymmetry and deviation from a sinusoidal CPR; in fact, numerical simulations (again with  $\lambda_L = 110$  nm) predict  $L = 1.2$  pH without edge damage and  $L = 5.4$  (2.6) pH with 20 (15) nm damage depth. With the measured  $I_{c,\max}^+ = 27$   $\mu$ A, those estimated inductance values result in  $\beta_L \approx 0.02$  without edge damage and 0.07 (0.03) with 20 (15) nm damage depth.

Figure 2(b) shows IVCs of the 2JJ-SoL recorded for both current-sweep directions before and after recutting, at values of  $I_{\text{mod}}$  that were adjusted to yield the critical currents  $I_{c,\max}^+$  and  $I_{c,\min}^+$ . Before recutting, both IVCs show a significant hysteresis, which we attribute to Joule heating effects. To reduce heating effects, we have recut the JJs to reduce their widths and, accordingly, their critical currents. As is evident from Fig. 2(b), the trimming of the JJs

strongly suppresses the hysteresis in the IVCs. This ability to controllably cut and recut features allows for a fine tunability of the SQUID-on-lever properties and demonstrates the robustness of the fabrication scheme.

Figure 2(c) shows a family of voltage  $V$  versus modulation current  $I_{\text{mod}}$  curves for different bias currents  $I$ , measured after recutting the 2JJ-SoL. We cannot find a shift of the voltage maxima along the  $I_{\text{mod}}$  axis with increasing  $I$ ; this indicates a negligible asymmetry in the SQUID inductance  $L$ . For  $|I_{\text{mod}}| \lesssim 0.5$  mA, the hysteresis in the IVCs causes the vertical switching steps in the  $V(I_{\text{mod}})$  curves, preventing operation of the SQUID in this regime. However, outside this regime ( $|I_{\text{mod}}| \gtrsim 0.5$  mA), the SQUID can be flux-biased via  $I_{\text{mod}}$  in a stable working point, and it can be operated as a flux-to-voltage transducer in a simple direct voltage readout scheme. For example, for  $I = 19$   $\mu$ A and  $I_{\text{mod}} = 0.72$  mA, a very high transfer function  $\partial V/\partial\Phi \equiv V_\Phi = 9$  mV/ $\Phi_0$  is reached. The integration of a modulation line in the SQUID-on-lever layout is an important feature, as it allows us to operate the sensor in its optimum working point and to use conventional SQUID readout electronics with FLL operation to maintain the optimum working point, even in a variable external magnetic field. We note, however, that  $I_{\text{mod}}$  in the milliamp range could be too invasive for some applications, as it can produce a disturbing magnetic field at the surface of a sample that is imaged. For example, a straight wire carrying 1 mA produces a Biot-Savart field of 4 mT at a radial distance of 50 nm. A solution of this problem can be provided by the 3JJ-SoLs.

Figure 3 summarizes results from measurements of two 3JJ-SoLs patterned with either Ne- or He-FIB milling,

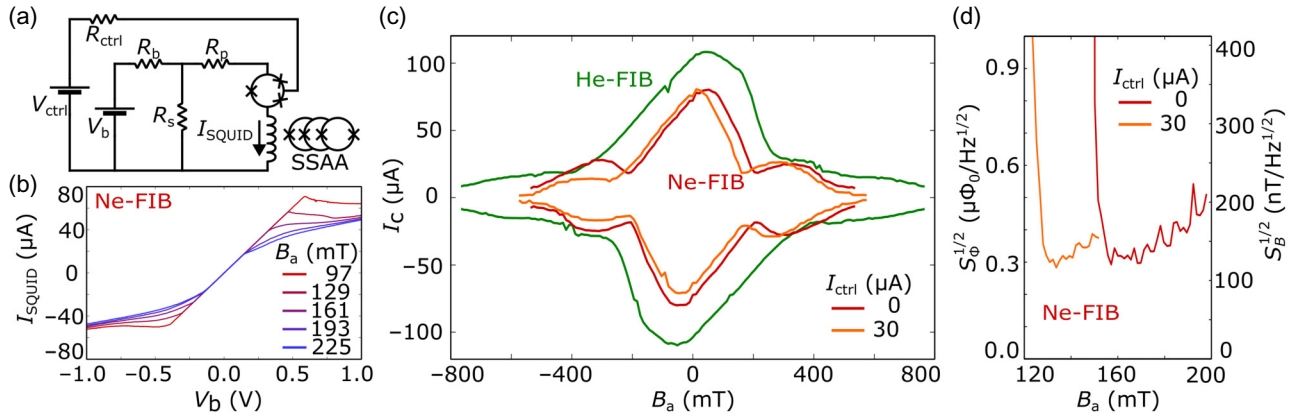


FIG. 3. Electric transport and noise properties of 3JJ-SoL. Results obtained at  $T = 4.2$  K with the configuration in (a) are shown in (b)–(d) for a 3JJ-SoL milled by Ne-FIB ( $w_1 = w_2 = 50$  nm,  $w_3 = 75$  nm); (c) also includes results from a 3JJ-SoL milled by He-FIB ( $w_1 = w_2 = 28$  nm,  $w_3 = 37$  nm), which was later used for imaging. Both devices have a hole diameter  $d = 15$  nm. (a) Readout circuit used for 3JJ-SoL characterization and imaging. (b)  $I_{\text{SQUID}}(V_b)$  curves at various magnetic fields  $B_a$ , with  $I_{\text{ctrl}} = 0$  for the 3JJ-SoL milled by Ne-FIB ( $R_b = 6.2$  k $\Omega$ ,  $R_s = 1$   $\Omega$ ). (c)  $I_c(B_a)$  for the 3JJ-SoL milled by He-FIB with  $I_{\text{ctrl}} = 0$  and for the 3JJ-SoL milled by Ne-FIB with  $I_{\text{ctrl}} = 0$  and 30  $\mu$ A. (d) Rms spectral densities of flux noise  $S_\Phi^{1/2}$  and field noise  $S_B^{1/2}$  at 12 kHz versus applied magnetic field  $B_a$  for the 3JJ-SoL milled by Ne-FIB. The two curves correspond to the most sensitive working points found with  $I_{\text{ctrl}} = 0$  at  $V_b = 0.15$  V and with  $I_{\text{ctrl}} = 30$   $\mu$ A at  $V_b = 0.4$  V.

both with hole diameter  $d = 15$  nm. For those devices, we did not trim the JJ widths to avoid hysteresis in the IVCs. Instead, we operated them using the readout scheme, shown in Fig. 3(a), which is implemented in the scanning SQUID microscope. This scheme allows for readout of a SQUID even if its IVC (with current bias) is hysteretic, which therefore enables SQUID operation over the widest possible magnetic field range [30,33]. This circuit operates the SQUIDs in voltage-bias mode at bias voltage  $V_b$ , with a large bias resistor  $R_b$ , a small shunt resistor  $R_s$ , and a parasitic resistance  $R_p$  (due to wires and contacts) in series with the SQUID;  $I_{\text{SQUID}}$  is measured with a serial SQUID array amplifier (SSAA), which is operated in FLL mode. A control current  $I_{\text{ctrl}}$  is applied via the voltage  $V_{\text{ctrl}}$  and resistor  $R_{\text{ctrl}}$ . The external magnetic field  $B_a$  is always applied perpendicular to the plane of the SQUID loop.

Figure 3(b) shows  $I_{\text{SQUID}}(V_b)$  of the 3JJ-SoL milled by Ne-FIB for different applied magnetic fields  $B_a$ , with  $I_{\text{ctrl}} = 0$ . For  $|I_{\text{SQUID}}| < I_c$ , the curves are linear, with an inverse slope  $V_b/I_{\text{SQUID}} \approx R_b(1 + R_p/R_s)$  (in the limit  $R_b \gg R_s, R_p$ ). From the measured  $V_b/I_{\text{SQUID}} = 8.06$  k $\Omega$ , we extract  $R_p = 0.3$   $\Omega$ . At the kinks in  $I_{\text{SQUID}}(V_b)$ , the critical current is reached. Figure 3(c) shows, for both 3JJ-SoLs (at  $I_{\text{ctrl}} = 0$ ), the  $I_c(B)$  curves that have been extracted from  $I_{\text{SQUID}}(V_b)$  data. The central maxima of the  $I_c(B)$  curves are shifted along the field axis, as expected from the asymmetry of a SQUID with three JJs [36]. The neighboring maxima are significantly suppressed for the 3JJ-SoL milled by Ne-FIB and almost absent for the 3JJ-SoL milled by He-FIB SQUID, owing to the decay of  $I_c$  as  $B$  approaches the upper critical field of the Nb film. This effect is a consequence of the small size of the SQUID and the resulting large SQUID oscillation period (equivalent to  $\Phi_0$ ), which corresponds to the difference  $\Delta B \approx 0.42$  T between the minima in  $I_c(B)$  for the Ne-FIB SQUID. This period, in turn, yields an effective area  $A_{\text{eff}} = \Phi_0/\Delta B \approx 4.92 \times 10^3$  nm<sup>2</sup>, corresponding to an effective diameter  $d_{\text{eff}} = (A_{\text{eff}} \cdot 4/\pi)^{1/2} \approx 80$  nm. For the 3JJ-SoL milled by He-FIB, we find  $\Delta B \approx 0.70$  T, resulting in  $d_{\text{eff}} \approx 60$  nm. For the 3JJ-SoL milled by Ne-FIB, we also show in Fig. 3(c) the  $I_c(B)$  curve obtained with  $I_{\text{ctrl}} = 30$   $\mu$ A, which is shifted by approximately  $-30$  mT along the  $B$  axis. This demonstrates an important feature of SQUIDs with three JJs: they provide the possibility of maintaining the optimum working point in variable magnetic fields by adjusting  $I_{\text{ctrl}}$ .

At selected working points ( $V_b, V_{\text{ctrl}}$ ), we measured the root-mean-square (rms) spectral density of current noise  $S_{I_{\text{SQUID}}}^{1/2}$  with the SSAA. Combined with the SQUID magnetic responses (transfer functions)  $\partial I_{\text{SQ}}/\partial \Phi$  and  $\partial I_{\text{SQ}}/\partial B$ , we determine the respective rms flux noise  $S_{\Phi}^{1/2} = S_{I_{\text{SQUID}}}^{1/2}/(\partial I_{\text{SQ}}/\partial \Phi)$  and field noise  $S_B^{1/2} = S_{I_{\text{SQUID}}}^{1/2}/(\partial I_{\text{SQ}}/\partial B)$ . Figure 3(d) shows measurements in the white noise limit at 12 kHz of  $S_{\Phi}^{1/2}$  (also converted

to  $S_B^{1/2}$ ) versus applied field for the 3JJ-SoL milled by Ne-FIB. We find a pronounced minimum in the flux noise of  $S_{\Phi}^{1/2} \approx 0.3 \mu\Phi_0/\sqrt{\text{Hz}}$ , corresponding to a field noise of  $S_B^{1/2} \approx 120$  nT/ $\sqrt{\text{Hz}}$ . The main reason for the minimum in flux noise (or field noise) is that, in this minimum, the SQUID has a maximum of its transfer function. For  $I_{\text{ctrl}} = 0$ , the minimum in noise versus  $B$  is at  $\sim 160$  mT. With  $I_{\text{ctrl}} = 30$   $\mu$ A, we can shift the optimum transfer function and hence the noise minimum to  $\sim 130$  mT. This again demonstrates the benefit of SQUIDs with three JJs: they provide the possibility of maintaining optimum sensitivity in variable magnetic fields via the adjustment of  $I_{\text{ctrl}}$ , which can be controlled by a PLL. Importantly, the amplitudes of  $I_{\text{ctrl}}$  required to shift the optimum working point in a magnetic field are about an order of magnitude lower than is required for  $I_{\text{mod}}$  for flux feedback in the case of a SQUID with two JJs. The smaller resulting stray fields make imaging with a 3JJ-SoL in a PLL less invasive than imaging with a 2JJ-SoL in a FLL.

#### IV. MAGNETIC IMAGING

To demonstrate the spatial resolution of magnetic microscopy with these SQUID-on-lever probes, we map the stray magnetic field at the surface of bulk  $\text{Cu}_2\text{OSeO}_3$ . At low temperature, this insulating cubic helimagnet hosts a number of modulated magnetic phases, including low-temperature skyrmion (LTS) and helical (H) phases, which produce nanometer-scale magnetic field patterns at the sample surface. In particular, in magnetic fields applied along  $\langle 100 \rangle$ , previous scanning SQUID microscopy has shown that the LTS phase appears on the corresponding  $\{100\}$  surface in the form of clusters of disordered skyrmions within a field-polarized (FP) background [43]. In images of the magnetic field, individual skyrmions generate a point-like reduction in the out-of-plane stray field, as a result of their core magnetization opposing the surrounding FP phase. Because of their small size—according to micromagnetic simulations, skyrmions in  $\text{Cu}_2\text{OSeO}_3$  have a radius of 10 nm to the region where their out-of-plane magnetization vanishes—these features are ideal for calibrating the point spread function of our scanning probe and determining its spatial resolution. For the experiments described next,  $I_{\text{ctrl}} = 0$  was used.

Figure 4(a) is a schematic of the SQUID-on-lever probe above the magnetization texture of a cluster of skyrmions within a FP background. To enter the LTS phase, we initially saturate the system with an out-of-plane applied magnetic field along  $[001]$  of  $\mu_0 H_z = 200$  mT at  $T = 5$  K. We then reverse this field, first applying  $-150$  mT, and map the stray magnetic field just above the  $(001)$  surface of the crystal. By measuring the response of the SQUID-on-lever sensor, we map the local magnetic field threading through the SQUID, i.e., the out-of-plane component of

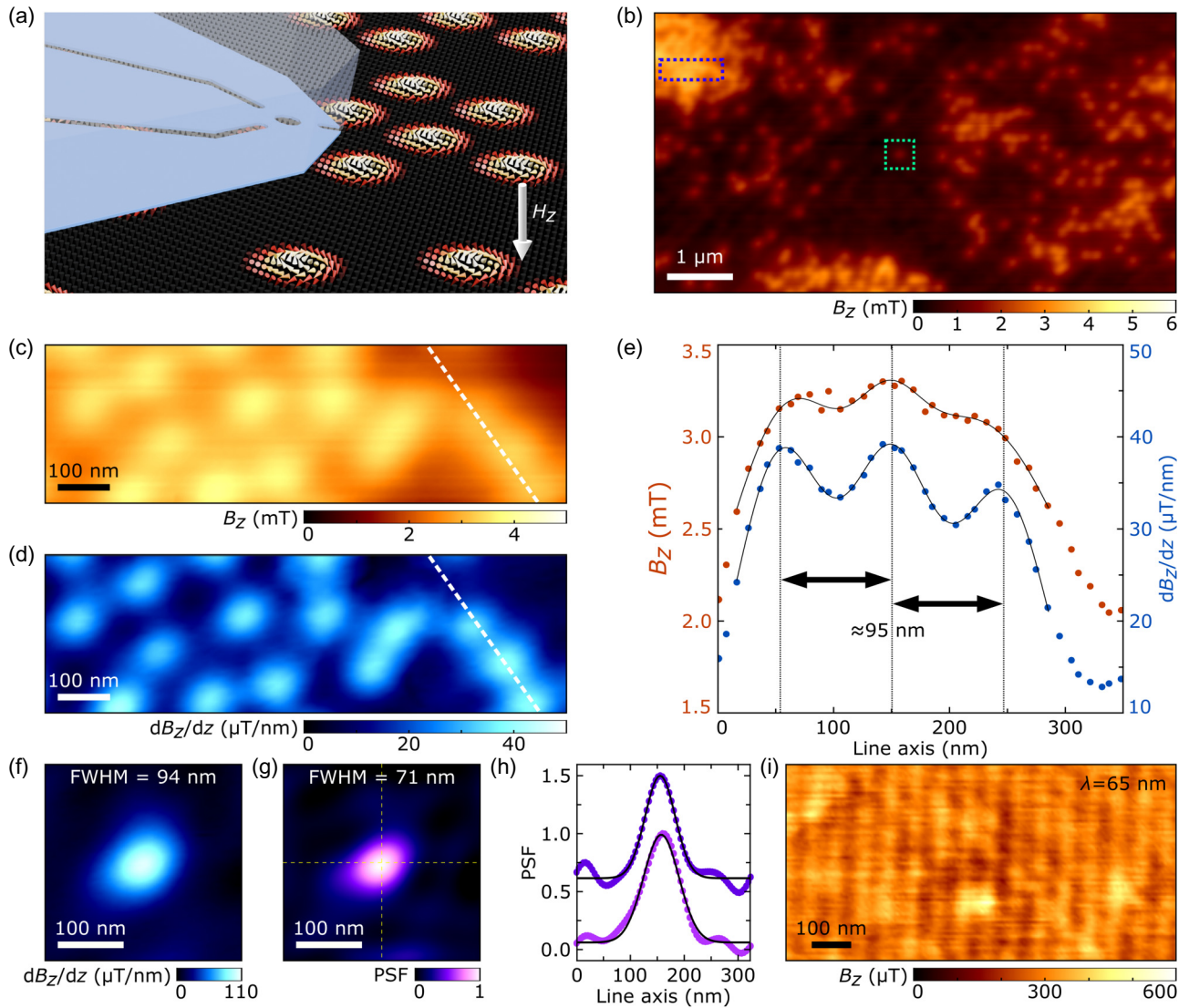


FIG. 4. Magnetic field microscopy. (a) Schematic of SQUID-on-lever scanning probe over skyrmions. (b)  $B_z(x, y)$  measured above  $\text{Cu}_2\text{OSeO}_3$  in the low-temperature skyrmion (LTS) phase at  $T = 5$  K. Blue and green dotted frames indicate the enlarged regions in (c, d) and (f, g), respectively. (c, d)  $B_z(x, y)$  and  $dB_z/dz(x, y)$  of skyrmion clusters. (e) Line cuts along the white dotted lines in (c, d). Points indicate measured data, while lines represent Gaussian fits. (f, g)  $dB_z/dz(x, y)$  and PSF of the SQUID-on-lever extracted from the measurement of a single skyrmion with 2D Gaussian fit FWHM. The PSF is centered on the SQUID loop at the end of the SQUID-on-lever probe, with the cantilever oriented along the  $x$ -axis with its tip facing right. (h) Line cuts along the dashed lines in (g). The vertical cut is offset by 0.5. Points indicate measured data, while lines represent Gaussian fits. (i)  $B_z(x, y)$  of the in-plane helical phase. Fourier space analysis yields a periodic spacing  $\lambda = 65 \pm 5$  nm. The SQUID-sample spacing was  $65 \pm 10$  nm for (b) to (e) and  $45 \pm 10$  nm for (f) to (i).

the magnetic field  $B_z(x, y)$ . We further oscillate the sample out of plane at a frequency of 177 Hz with amplitude  $\Delta z \approx 4.3$  nm and use a lock-in amplifier to map the ac field  $B_{ac}(x, y)$ . To first-order,  $B_{ac} \approx \Delta z \cdot dB_z/dz$  and thus provides a measure of the out-of-plane field gradient threading the SQUID. We image the near-surface stray field as a function of increasing reverse field. At  $-155$  mT, images show the coexistence of domains of tilted spiral phase, FP phase, and clusters of LTS phase, as expected from previous measurements [43]. At  $-160$  mT, only clusters

of skyrmions remain in an FP background, as shown in Fig. 4(b).

Figures 4(c) and 4(d) focus on a dense cluster of skyrmions, highlighted by the blue rectangle in (b), showing  $B_z(x, y)$  and  $dB_z/dz(x, y)$ , respectively. As in Fig. 4(b), data have been obtained for a constant SQUID-sample spacing of  $65 \pm 10$  nm. From the partially overlapping features, the superior resolution of the  $dB_z/dz(x, y)$  image, compared with the  $B_z(x, y)$  image, is clear. This improvement results from a combination of both the higher spatial

resolution characteristic of measuring a magnetic field derivative, compared with a magnetic field [44], and the noise reduction offered by the spectral filtering of the lock-in-based derivative measurement. Line cuts through the images along the white dotted lines, shown in Fig. 4(e), cut across a row of three nearby skyrmions. These skyrmions, which are separated by about 95 nm, are resolved in both the field and field-derivative measurements, although their separation in the latter is more evident. A common definition of spatial resolution is the smallest distance between two point-like objects for which each appears distinct. Under the Sparrow criterion, this distance can be defined as the separation below which the minimum between two point-like features disappears. Given the clearly defined minima in the field-derivative measurement and the fact that the stray field produced by the individual skyrmions in the scanning plane is not point-like, these images demonstrate that the SQUID-on-lever is capable of spatial resolution well below 100 nm.

Figure 4(f) shows the contrast of a single skyrmion, highlighted by the green square in (b) and measured at a constant SQUID-sample spacing of  $45 \pm 10$  nm. By fitting the  $B_z(x, y)$  and  $dB_z/dz(x, y)$  profiles with Gaussian functions, we find full widths at half maximum (FWHMs) of 130 and 94 nm, respectively [only  $dB_z/dz(x, y)$  is shown in Fig. 4(f)]. Given that the SQUID does not measure magnetic field at each point in space, but rather measures the integrated magnetic flux threading through its diameter, its response to a spatially varying magnetic field is characterized by a point spread function (PSF). Slight asymmetries in this PSF, resulting from the shape of the particular SQUID-on-lever sensor, probably result in the asymmetry visible in the images of the skyrmion, whose field profile should be circularly symmetric.

To determine the PSF of our SQUID-on-lever probe, we compare  $dB_z/dz(x, y)$  images of a single skyrmion, measured using the SQUID, with the idealized stray field expected for a skyrmion in  $\text{Cu}_2\text{OSeO}_3$ . We simulate this stray field above the surface of the sample using the micromagnetic software package MUMAX3, which is based on the Landau-Lifshitz-Gilbert formalism [45,46]. We then use an iterative Landweber algorithm to extract a PSF from the simulated and measured stray-field images. The algorithm starts from an initial estimate of the PSF, which, after each step, is successively improved on by reducing the error between the measured stray-field image and that generated by convolving the simulated stray field with the PSF. The algorithm converges once this error is comparable to the measurement noise [47]. The PSF extracted from the  $dB_z/dz(x, y)$  map of the single skyrmion in Fig. 4(f) is shown in Fig. 4(g). This point spread function, as shown by the horizontal and vertical line cuts and fits in Fig. 4(h), is approximately Gaussian and has a FWHM of 71 nm, giving another measure of the probe's spatial resolution. Given the similar size of the point spread function and the

measured  $dB_z/dz(x, y)$  profile of the single skyrmion, it is clear that the field profile of the skyrmion itself at this tip-sample spacing is much smaller than the resolution of our probe. In that sense, the images in Figs. 4(f) and 4(g) reveal the size and asymmetries of the SQUID-on-lever probe, rather than features related to the skyrmion's stray field.

As a further test of the probe's response to small magnetic features, we also image the short-wavelength magnetic modulation produced by an in-plane H phase, again at a constant SQUID-sample spacing of  $45 \pm 10$  nm. At low temperature and in low applied magnetic fields,  $\text{Cu}_2\text{OSeO}_3$  can enter a multidomain H phase, in which domains of magnetization helices, which propagate along [100], [010], or [001], coexist. At a {100} surface, in-plane H domains appear as sinusoidal stray-field modulations, with a period given by the wavelength of the intrinsic helimagnetic order in  $\text{Cu}_2\text{OSeO}_3$ ,  $\lambda_m = 62$  nm [43,48]. To produce in-plane H domains at the sample surface, we apply an in-plane magnetic field  $\mu_0 H_x = 200$  mT, aligned approximately along [100] to fully polarize the sample at  $T = 5$  K. We then decrease the applied field to less than 12 mT and make maps of  $B_z(x, y)$  above the surface. A characteristic image is shown in Fig. 4(g), revealing a sinusoidal stray-field modulation with a period of  $\lambda = 65 \pm 5$  nm propagating along [100]. The error in the measurement of the period is due to a systematic uncertainty in our calibration of the piezoelectric scanner used to scan the sample. Apart from nonperiodic modulations in the  $B_z(x, y)$  maps, which are due to surface roughness, the images are consistent with behavior expected from the stray field at the surface of an in-plane H phase. The clarity of the contrast provides a final confirmation of the SQUID-on-lever's sensitivity to spatial variations in magnetic field on length scales smaller than 100 nm.

## V. CONCLUSION

We demonstrate a method for fabricating robust SQUID-on-lever probes for high-sensitivity SSM. These probes combine the advantages of previously developed SQUID-on-chip and SQUID-on-tip devices: the large-scale fabrication, robustness, and on-chip circuitry of the former; the sub-100-nm spatial resolution, critical fields exceeding 0.5 T, and local thermal sensitivity of the latter; and the high magnetic field sensitivity of both. In addition, SQUID-on-lever sensors offer the tip-sample distance control and topographic contrast of noncontact AFM. By imaging nanometer-scale magnetization textures, we determine the probe's point spread function and demonstrate its ability to resolve features spaced by less than 100 nm. Images of a modulated magnetization pattern with a period of 65 nm further demonstrate the probe's sensitivity to magnetic field variations with short spatial wavelengths.

SQUID-on-lever probes with integrated modulation lines or control lines could be operated in a flux-locked or phase-locked loop mode to extend their range of sensitivity in a magnetic field, reducing “blind spots,” i.e., ranges of magnetic field where the SQUID is insensitive [37]. All of these properties, combined with the ease of use of the cantilever platform and the robustness of the probes, will dramatically expand the application of nanometer-scale SSM in the fields of magnetism, superconductivity, and low-temperature transport.

### ACKNOWLEDGMENTS

We thank Professor Kam Moler for helpful discussions. We acknowledge support by the European Commission under H2020 FET Open Grant “FIBsuperProbes” (Grant No. 892427) and the Swiss National Science Foundation under Grant No. 200020-207933. We also gratefully acknowledge support by the COST actions NANOCOBYBRI (CA16218), FIT4NANO (CA19140), and SUPERQUMAP (CA21144).

### DATA AVAILABILITY

The data that support the findings of this article are not publicly available. The data are available from the authors on reasonable request.

### APPENDIX A: $\text{Cu}_2\text{OSeO}_3$ SAMPLE

The  $\text{Cu}_2\text{OSeO}_3$  crystal is grown via chemical vapor transport with  $\text{CuO}$  and  $\text{SeO}_2$  as starting materials and  $\text{HCl}$  as the transport agent [49]. A well-faceted single crystal is chosen with a natural  $\{100\}$  facet. The orientation is verified using a Laue camera. The facet is then mechanically polished and the orientation is subsequently reverified using the Laue camera. Miscut angles are measured using rocking curves with X-ray diffraction and found to be less than  $1^\circ$ .

### APPENDIX B: SCANNING SQUID MICROSCOPY

We perform both noncontact AFM and SSM using SQUID-on-lever probes in a custom-built microscope under high vacuum inside a  $^4\text{He}$  cryostat at 4.2 K [33]. The microscope contains a vector magnet that can apply a field of up to 1 T either in or out of plane, i.e., along  $\hat{x}$  or  $\hat{z}$ .

Piezoelectric walkers and scanners (Attocube ANPx 311/LT/HV, ANSxy100lr/LT/HV) are used to move the sample. The cantilever’s flexural motion is monitored by a fiber-optic interferometer, consisting of a 1550-nm diode laser (Toptica), a 95:5 fiber-optic coupler, and a custom-built objective, focusing light onto the cantilever to an 8- $\mu\text{m}$  spot. Interference from the low-finesse Fabry-Pérot interferometer formed by the cleaved face of the optical fiber and the cantilever shaft is measured by a photoreceiver with an effective 3-dB bandwidth of 800 kHz.

The cavity is stabilized against drift using a proportional-integral-derivative controller to control the laser temperature. The incident power of around  $1\ \mu\text{W}$  does not significantly heat the SQUID-on-lever probe, as confirmed by measurements of its superconducting properties. The cantilever is excited to an amplitude of 10 nm at its fundamental mechanical resonance frequency by a piezoelectric actuator driven by a phase-locked loop (Nanonis BP5e). At 4.2 K and in high vacuum, the cantilever has a resonance frequency of 577 kHz and a mechanical quality factor of 15 000.

To image the sample, we control the SQUID-on-lever probe to approach the surface while monitoring the cantilever’s mechanical resonance. Shifts are observed at tip-sample spacings exceeding 500 nm, allowing for a controlled approach. We identify the point at which the cantilever makes contact with the surface using the onset of strongly repulsive tip-sample forces, which result in both a positive shift of the cantilever’s mechanical frequency and its deflection. The SQUID-on-lever probe is mounted at a  $10^\circ$  angle with respect to the sample surface, such that the end of the cantilever is the first part to come into contact with the sample. On contact, the SQUID loop itself, which is set back from the end of the lever, remains some distance above the sample surface (this value is of the order of 20 nm, but depends on the precise design of the individual SQUID-on-lever). We then retract the tip from contact to a constant tip-sample spacing during imaging.

The SQUID is characterized and operated in a semi-voltage-biased circuit, in which the current response  $I_{\text{SQUID}}$  is measured by a series SQUID array amplifier (Magnicon). We calibrate the SQUID’s response to a magnetic field by measuring  $I_{\text{SQUID}}$  versus  $\mu_0 H_z$  before and after each scan in a field range significantly larger than the field created by the  $\text{Cu}_2\text{OSeO}_3$ .

### APPENDIX C: MICROMAGNETIC SIMULATIONS

We use the finite-element software package MUMAX3 [45,46], which is based on the Landau-Lifshitz-Gilbert formalism, to simulate the magnetization profile of individual skyrmions in  $\text{Cu}_2\text{OSeO}_3$ . As simulation parameters, we use a saturation magnetization of 103 kA/m, an exchange stiffness of 0.35 pJ/m, a bulk Dzyaloshinskii-Moriya constant of  $0.74\ \mu\text{J}/\text{m}^2$ , and a cubic anisotropy constant of  $1.2\ \text{kJ}/\text{m}^3$ . Cubic anisotropy axes point along the axes of the  $xyz$  coordinate system. To mimic the geometry of a bulk piece of single-crystal  $\text{Cu}_2\text{OSeO}_3$ , we employ periodic boundary conditions in  $x$  and  $y$ , with five repetitions on each side of a simulation volume of  $1008 \times 1008 \times 200\ \text{nm}^3$ . The finite-element mesh is set to a size of  $240 \times 240 \times 40$  cells with corresponding cell sizes of  $4.2 \times 4.2 \times 5\ \text{nm}^3$ , respectively. To facilitate the stable appearance of individual skyrmions, we apply a constant, homogeneous, magnetic field along  $\hat{z}$  with a

strength of 0.2 T, and initiate the magnetization with a Bloch skyrmion, which has its core pointing along  $\hat{z}$  in the center of the simulation volume. We then relax the system to the next energetic minimum that is found by the solver.

- 
- [1] D. V. Christensen, *et al.*, 2024 roadmap on magnetic microscopy techniques and their applications in materials science, *J. Phys.: Mater.* **7**, 032501 (2024).
- [2] D. Vasyukov, L. Ceccarelli, M. Wyss, B. Gross, A. Schwarb, A. Mehlin, N. Rossi, G. Tütüncüoğlu, F. Heimbach, R. R. Zamani, A. Kovács, A. Fontcuberta i Morral, D. Grundler, and M. Poggio, Imaging stray magnetic field of individual ferromagnetic nanotubes, *Nano Lett.* **18**, 964 (2018).
- [3] M. Wyss, S. Gliga, D. Vasyukov, L. Ceccarelli, G. Romagnoli, J. Cui, A. Kleibert, R. L. Stamps, and M. Poggio, Stray-field imaging of a chiral artificial spin ice during magnetization reversal, *ACS Nano* **13**, 13910 (2019).
- [4] J. A. Bert, B. Kalisky, C. Bell, M. Kim, Y. Hikita, H. Y. Hwang, and K. A. Moler, Direct imaging of the coexistence of ferromagnetism and superconductivity at the LaAlO<sub>3</sub>/SrTiO<sub>3</sub> interface, *Nat. Phys.* **7**, 767 (2011).
- [5] D. V. Christensen, Y. Frenkel, Y. Z. Chen, Y. W. Xie, Z. Y. Chen, Y. Hikita, A. Smith, L. Klein, H. Y. Hwang, N. Pryds, and B. Kalisky, Strain-tunable magnetism at oxide domain walls, *Nat. Phys.* **15**, 269 (2019).
- [6] X. R. Wang, C. J. Li, W. M. Lü, T. R. Paudel, D. P. Leusink, M. Hoek, N. Poccia, A. Vailionis, T. Venkatesan, J. M. D. Coey, E. Y. Tsybal, Ariando, and H. Hilgenkamp, Imaging and control of ferromagnetism in LaMnO<sub>3</sub>/SrTiO<sub>3</sub> heterostructures, *Science* **349**, 716 (2015).
- [7] E. O. Lachman, A. F. Young, A. Richardella, J. Cuppens, H. R. Naren, Y. Anahory, A. Y. Meltzer, A. Kandala, S. Kempinger, Y. Myasoedov, M. E. Huber, N. Samarth, and E. Zeldov, Visualization of superparamagnetic dynamics in magnetic topological insulators, *Sci. Adv.* **1**, e1500740 (2015).
- [8] A. Noah, Y. Zur, N. Fridman, S. Singh, A. Gutfreund, E. Herrera, A. Vakahi, S. Remennik, M. E. Huber, S. Gazit, H. Suderow, H. Steinberg, O. Millo, and Y. Anahory, Nano-patterned magnetic edges in CrGeTe<sub>3</sub> for quasi 1-D spintronic devices, *ACS Appl. Nano Mater.* **6**, 8627 (2023).
- [9] Y. Zur, A. Noah, C. Boix-Constant, S. Mañas-Valero, N. Fridman, R. Rama-Eiroa, M. E. Huber, E. J. G. Santos, E. Coronado, and Y. Anahory, Magnetic imaging and domain nucleation in CrSBr down to the 2D limit, *Adv. Mater.* **35**, 2307195 (2023).
- [10] A. Vervelaki, K. Bagani, D. Jetter, M.-H. Doan, T. K. Chau, B. Gross, D. V. Christensen, P. Bøggild, and M. Poggio, Visualizing thickness-dependent magnetic textures in few-layer Cr<sub>2</sub>Ge<sub>2</sub>Te<sub>6</sub>, *Commun. Mater.* **5**, 40 (2024).
- [11] K. Bagani, A. Vervelaki, D. Jetter, A. Devarakonda, M. A. Tschudin, B. Gross, D. G. Chica, D. A. Broadway, C. R. Dean, X. Roy, P. Maletinsky, and M. Poggio, Imaging strain-controlled magnetic reversal in thin CrSBr, *Nano Lett.* **24**, 13068 (2024).
- [12] C. L. Tschirhart, M. Serlin, H. Polshyn, A. Shragai, Z. Xia, J. Zhu, Y. Zhang, K. Watanabe, T. Taniguchi, M. E. Huber, and A. F. Young, Imaging orbital ferromagnetism in a moiré Chern insulator, *Science* **372**, 1323 (2021).
- [13] K. C. Nowack, E. M. Spanton, M. Baenninger, M. König, J. R. Kirtley, B. Kalisky, C. Ames, P. Leubner, C. Brüne, H. Buhmann, L. W. Molenkamp, D. Goldhaber-Gordon, and K. A. Moler, Imaging currents in HgTe quantum wells in the quantum spin Hall regime, *Nat. Mater.* **12**, 787 (2013).
- [14] G. M. Ferguson, R. Xiao, A. R. Richardella, D. Low, N. Samarth, and K. C. Nowack, Direct visualization of electronic transport in a quantum anomalous Hall insulator, *Nat. Mater.* **22**, 1100 (2023).
- [15] A. Uri, Y. Kim, K. Bagani, C. K. Lewandowski, S. Grover, N. Auerbach, E. O. Lachman, Y. Myasoedov, T. Taniguchi, K. Watanabe, J. Smet, and E. Zeldov, Nanoscale imaging of equilibrium quantum Hall edge currents and of the magnetic monopole response in graphene, *Nat. Phys.* **16**, 164 (2020).
- [16] A. Uri, S. Grover, Y. Cao, J. A. Crosse, K. Bagani, D. Rodan-Legrain, Y. Myasoedov, K. Watanabe, T. Taniguchi, P. Moon, M. Koshino, P. Jarillo-Herrero, and E. Zeldov, Mapping the twist-angle disorder and Landau levels in magic-angle graphene, *Nature* **581**, 47 (2020).
- [17] B. Kalisky, E. M. Spanton, H. Noad, J. R. Kirtley, K. C. Nowack, C. Bell, H. K. Sato, M. Hosoda, Y. Xie, Y. Hikita, C. Woltmann, G. Pfanzelt, R. Jany, C. Richter, H. Y. Hwang, J. Mannhart, and K. A. Moler, Locally enhanced conductivity due to the tetragonal domain structure in LaAlO<sub>3</sub>/SrTiO<sub>3</sub> heterointerfaces, *Nat. Mater.* **12**, 1091 (2013).
- [18] A. Aharon-Steinberg, T. Völkl, A. Kaplan, A. K. Pariari, I. Roy, T. Holder, Y. Wolf, A. Y. Meltzer, Y. Myasoedov, M. E. Huber, B. Yan, G. Falkovich, L. S. Levitov, M. Hücker, and E. Zeldov, Direct observation of vortices in an electron fluid, *Nature* **607**, 74 (2022).
- [19] E. Persky, I. Sochnikov, and B. Kalisky, Studying quantum materials with scanning SQUID microscopy, *Annu. Rev. Condens. Matter Phys.* **13**, 385 (2022).
- [20] J. R. Kirtley, Fundamental studies of superconductors using scanning magnetic imaging, *Rep. Progr. Phys.* **73**, 126501 (2010).
- [21] L. Embon, Y. Anahory, Ž. L. Jelić, E. O. Lachman, Y. Myasoedov, M. E. Huber, G. P. Mikitik, A. V. Silhanek, M. V. Milošević, A. Gurevich, and E. Zeldov, Imaging of superfast dynamics and flow instabilities of superconducting vortices, *Nat. Commun.* **8**, 85 (2017).
- [22] A. Kremen, H. Khan, Y. L. Loh, T. I. Baturina, N. Trivedi, A. Frydman, and B. Kalisky, Imaging quantum fluctuations near criticality, *Nat. Phys.* **14**, 1205 (2018).
- [23] E. Persky, A. V. Bjørllig, I. Feldman, A. Almoalem, E. Altman, E. Berg, I. Kimchi, J. Ruhman, A. Kanigel, and B. Kalisky, Magnetic memory and spontaneous vortices in a van der Waals superconductor, *Nature* **607**, 692 (2022).
- [24] Y. Iguchi, R. A. Shi, K. Kihou, C.-H. Lee, M. Barkman, A. L. Benfenati, V. Grinenko, E. Babaev, and K. A. Moler, Superconducting vortices carrying a temperature-dependent fraction of the flux quantum, *Science* **380**, 1244 (2023).
- [25] J. R. Kirtley, M. B. Ketchen, K. G. Stawiasz, J. Z. Sun, W. J. Gallagher, S. H. Blanton, and S. J. Wind, High-resolution

- scanning SQUID microscope, *Appl. Phys. Lett.* **66**, 1138 (1995).
- [26] N. C. Koshnick, M. E. Huber, J. A. Bert, C. W. Hicks, J. Large, H. Edwards, and K. A. Moler, A terraced scanning superconducting quantum interference device susceptometer with submicron pickup loops, *Appl. Phys. Lett.* **93**, 243101 (2008).
- [27] J. R. Kirtley, L. Paulius, A. J. Rosenberg, J. C. Palmstrom, C. M. Holland, E. M. Spanton, D. Schiessl, C. L. Jermain, J. Gibbons, Y.-K.-K. Fung, M. E. Huber, D. C. Ralph, M. B. Ketchen, G. W. Gibson, and K. A. Moler, Scanning SQUID susceptometers with sub-micron spatial resolution, *Rev. Sci. Instrum.* **87**, 093702 (2016).
- [28] M. E. Huber, N. C. Koshnick, H. Bluhm, L. J. Archuleta, T. Azaa, P. G. Björnsson, B. W. Gardner, S. T. Halloran, E. A. Lucero, and K. A. Moler, Gradiometric micro-SQUID susceptometer for scanning measurements of mesoscopic samples, *Rev. Sci. Instrum.* **79**, 053704 (2008).
- [29] A. Finkler, Y. Segev, Y. Myasoedov, M. L. Rappaport, L. Ne'eman, D. Vasyukov, E. Zeldov, M. E. Huber, J. Martin, and A. Yacoby, Self-aligned nanoscale SQUID on a tip, *Nano Lett.* **10**, 1046 (2010).
- [30] D. Vasyukov, Y. Anahory, L. Embon, D. Halbertal, J. Cuppens, L. Neeman, A. Finkler, Y. Segev, Y. Myasoedov, M. L. Rappaport, M. E. Huber, and E. Zeldov, A scanning superconducting quantum interference device with single electron spin sensitivity, *Nat. Nanotechnol.* **8**, 639 (2013).
- [31] K. Bagani, J. Sarkar, A. Uri, M. L. Rappaport, M. E. Huber, E. Zeldov, and Y. Myasoedov, Sputtered  $\text{Mo}_{66}\text{Re}_{34}$  SQUID-on-tip for high-field magnetic and thermal nanoimaging, *Phys. Rev. Appl.* **12**, 044062 (2019).
- [32] M. José Martínez-Pérez and D. Koelle, NanoSQUIDs: Basics & recent advances, *Phys. Sci. Rev.* **2**, 20175001 (2017).
- [33] M. Wyss, K. Bagani, D. Jetter, E. Marchiori, A. Vervelaki, B. Gross, J. Ridderbos, S. Gliga, C. Schönenberger, and M. Poggio, Magnetic, thermal, and topographic imaging with a nanometer-scale SQUID-on-lever scanning probe, *Phys. Rev. Appl.* **17**, 034002 (2022).
- [34] M. Rog, T. J. Blom, D. B. Boltje, J. D. de Haan, R. Fermin, J. Niu, Y. C. Doedes, M. P. Allan, and K. Lahabi, Tapping-mode SQUID-on-tip microscopy with proximity Josephson junctions, *ArXiv:2508.21575*.
- [35] T. Weber, L. Cadorim, M. V. Milošević, R. Kleiner, and D. Koelle, Niobium Dayem bridges fabricated by Ne and He focused ion beams (Unpublished).
- [36] A. Y. Meltzer, A. Uri, and E. Zeldov, Multi-terminal multi-junction dc SQUID for nanoscale magnetometry, *Supercond. Sci. Technol.* **29**, 114001 (2016).
- [37] A. Uri, A. Y. Meltzer, Y. Anahory, L. Embon, E. O. Lachman, D. Halbertal, N. HR, Y. Myasoedov, M. E. Huber, A. F. Young, and E. Zeldov, Electrically tunable multiterminal SQUID-on-tip, *Nano Lett.* **16**, 6910 (2016).
- [38] S. Wolter, J. Linek, T. Weimann, D. Koelle, R. Kleiner, and O. Kieler, Static and dynamic transport properties of multi-terminal, multi-junction microSQUIDs realized with Nb/HfTi/Nb Josephson junctions, *Supercond. Sci. Technol.* **35**, 085006 (2022).
- [39] C. D. Tesche and J. Clarke, dc SQUID: Noise and optimization, *J. Low Temp. Phys.* **29**, 301 (1977).
- [40] B. Chesca, R. Kleiner, and D. Koelle, in *The SQUID Handbook* (Wiley, Weinheim, 2004), p. 29.
- [41] J. R. Prance and M. D. Thompson, Sensitivity of a dc SQUID with a non-sinusoidal current-phase relation in its junctions, *Appl. Phys. Lett.* **122**, 222601 (2023).
- [42] M. M. Khapaev, M. Y. Kupriyanov, E. Goldobin, and M. Siegel, Current distribution simulation for superconducting multi-layered structures, *Supercond. Sci. Technol.* **16**, 24 (2002).
- [43] E. Marchiori, G. Romagnoli, L. Schneider, B. Gross, P. Sahafi, A. Jordan, R. Budakian, P. R. Baral, A. Magrez, J. S. White, and M. Poggio, Imaging magnetic spiral phases, skyrmion clusters, and skyrmion displacements at the surface of bulk  $\text{Cu}_2\text{OSeO}_3$ , *Commun. Mater.* **5**, 202 (2024).
- [44] E. Marchiori, L. Ceccarelli, N. Rossi, L. Lorenzelli, C. L. Degen, and M. Poggio, Nanoscale magnetic field imaging for 2D materials, *Nat. Rev. Phys.* **4**, 49 (2022).
- [45] A. Vansteenkiste, J. Leliaert, M. Dvornik, M. Helsen, F. Garcia-Sanchez, and B. Van Waeyenberge, The design and verification of MUMAX3, *AIP Adv.* **4**, 107133 (2014).
- [46] L. Exl, S. Bance, F. Reichel, T. Schrefl, H. Peter Stimming, and N. J. Mauser, LaBonte's method revisited: An effective steepest descent method for micromagnetic energy minimization, *J. Appl. Phys.* **115**, 17D118 (2014).
- [47] P. L. Combettes and J.-C. Pesquet, in *Fixed-Point Algorithms for Inverse Problems in Science and Engineering*, edited by H. H. Bauschke, R. S. Burachik, P. L. Combettes, V. Elser, D. R. Luke, and H. Wolkowicz (Springer New York, New York, NY, 2011), p. 185.
- [48] T. Adams, A. Chacon, M. Wagner, A. Bauer, G. Brandl, B. Pedersen, H. Berger, P. Lemmens, and C. Pfleiderer, Long-wavelength helimagnetic order and skyrmion lattice phase in  $\text{Cu}_2\text{OSeO}_3$ , *Phys. Rev. Lett.* **108**, 237204 (2012).
- [49] P. R. Baral, V. Ukleev, T. LaGrange, R. Cubitt, I. Živković, H. M. Rønnow, J. S. White, and A. Magrez, Tuning topological spin textures in size-tailored chiral magnet insulator particles, *J. Phys. Chem. C* **126**, 11855 (2022).